Model Predictive Control With Duty Ratio Modulation for Open-Winding PMSM Drives With Common DC Bus

Xueping Li, Shuo Zhang, *Member, IEEE*, Chengning Zhang, Ying Zhou, Xin Yuan, *Member, IEEE*, and Yuelin Dong

***Abstract*—Finite control set model predictive current control (FCS–MPCC) has attracted increasing attention in recent years. However, large current ripples, torque ripples, and computational effort limit its widespread application. To address aforementioned problems, an improved MPCC method is proposed for open-winding permanent magnet synchronous motors herein. First, FCS–MPCC method based on deadbeat principle (FCS–MPCC–DB) is presented to reduce the computational effort. During the process, zero-sequence voltage is considered separately, avoiding enumerating all feasible voltage vectors (VVs). Second, an optimization strategy is proposed to reduce current ripples, torque ripples, and suppress zero-sequence current simultaneously. The switching state of one of two voltage-source inverters (VSIs) system is fixed, and the optimal vector duration ratios of the other VSI are obtained from a novel cost function. In other words, only one VSI system applies a fixed switching state, and a zero VV and an active VV are applied in the other VSI, so we name it half-FCS–MPCC–DB. Finally, several simulation and experimental results are presented to prove the effectiveness of proposed method.**

***Index Terms*—Deadbeat (DB) control, model predictive current control (MPCC), open-winding permanent magnet synchronous motor (OW-PMSM).**

I. Introduction

THE permanent magnet synchronous motor (PMSM) has been applied in many fields owing to its high torque density, high efficiency, and high-power density [1]. Recently, open-winding PMSM (OW-PMSM) has obtained plenty of attention because of its many merits, such as open-circuit fault tolerance, multilevel output voltage, and high dc bus utilization, compared to traditional PMSM [2].

Manuscript received 31 December 2022; revised 11 June 2023 and 19 July 2023; accepted 22 August 2023. Date of publication 28 August 2023; date of current version 23 October 2023. This work was supported by the High-efficiency cooling design and suppression technology of vibration and noise for high-speed and high-power density PMSM under Grant 2022YFB2502702. Recommended for publication by Associate Editor B. Semail. *(Corresponding author: Shuo Zhang.)*

Xueping Li, Shuo Zhang, Chengning Zhang, Ying Zhou, and Yuelin Dong are with the School of Mechanical Engineering and Collaborative Innovation Center of Electric Vehicles in Beijing, Beijing Institute of Technology, Beijing 100081, China (e-mail: lixueping6677@163.com; shuozhangxd@gmail.com; mrzhchn@bit.edu.cn; zhouying6369@163.com; dongyuelin517@163.com).

Xin Yuan is with the Department of Electrical and Electronic Engineering, The Hong Kong Polytechnic University, Hong Kong (e-mail: xinyuan@polyu.edu.hk).

Color versions of one or more figures in this article are available at https://doi.org/10.1109/TPEL.2023.3308892.

Digital Object Identifier 10.1109/TPEL.2023.3308892

In terms of power supply modes, OW-PMSM drive systems can be divided into two categories, namely the common dc bus topology [3] and the isolated dc bus topology [4]. The topology with isolated dc bus always has more weight and higher cost, so systems with a common dc bus is applied in some fields with requirements of power density and cost [5].

However, zero-sequence loop (ZSL) exists in the topology with common dc bus. The zero-sequence current (ZSC) in ZSL could reduce the efficiency of the system, so it should be suppressed [6].

With the development of powerful digital controller, many advanced control methods are implemented in drive system. Since model predictive control (MPC) method has a satisfactory dynamic and steady-state performance, it has been studied recently [7]. Based on if there exists a modulator, MPC can be classified into two groups: continuous control set MPC [8] and finite control set MPC (FCS–MPC) [9]. In FCS–MPC, a cost function, which synthesizes the control objectives, is defined to choose optimal voltage vector (VV) among all available vectors. The concept of FCS–MPC is easy to understand and the method is easy to implement [10]. However, all feasible VVs are enumerated, which means large calculational effort, especially multistep prediction is implemented [11]. In traditional PMSM, there are only eight VVs. However, because the existence of dual inverters, the number of VVs of OW-PMSM is up to 64. Even overlook redundant vectors, there are still 27 VVs. The more VVs always means long computation time, and then sampling frequency is restricted, which influences the performance of the control system. Meanwhile, large current and torque ripples also exist in FCS–MPC [12]. To solve the aforementioned problems, many control strategies have been studied.

To reduce the computational effort, two lookup tables are established based on torque deviation and the positions of voltage and stator flux. As a result, the number of candidate VVs is reduced from 27 to 10, which relieves the computational burden effectively [13]. In [14], an improved prediction method based on a new cost function is proposed and it addresses the complex tunning work of weighting factors. Since it is focused on OW-PMSM with isolated dc bus drive system, the problem of ZSC suppression is not taken into consideration, and it cannot be applied to OW-PMSM with a common dc bus topology directly. Zhu et al. [15] presented a novel FCS–MPC based on A-B-C frame to avoid weighting factors, resulting in a total of

nine evaluations to find the optimal VVs. The authors in [16], [17], and [18] used sector distribution strategy to reduce the number of available VVs to reduce computational burden. In [16], the FCS model predictive torque control is combined with deadbeat (DB) control principle. According to DB, the desired voltage of next instant is calculated and only few VVs adjacent with it are considered as candidate VVs, avoiding the complete enumeration for testing all feasible VVs. Different from [16], the FCS model predictive current control (FCS–MPCC) is proposed in [17], of which control variables are currents. In [18], the whole voltage plane is divided in 24 triangles to reduce the calculation of possible cost functions. Compared to traditional FCS–MPC, the calculation time of [13], [14], [15], [16], [17], and [18] has reduced clearly; however, the large current and torque ripples still exist in these systems.

To reduce current and torque ripples, a duty cycle control strategy using more than only one VV in one control period is proposed in [19], [20], [21], [22], and [23]. In [19], an active selected VV and one zero VV is used in each interval, which has a good performance in reducing torque ripples. In [20], two active VVs and one zero VV are applied in one control period. To minimize the error between the desired VV and the synthesis VV, the duration ratios of optimal vector can be obtained from the cost function, then switching sequence is obtained. It is also effective in reducing current ripples. But both [19] and [20] are aimed at traditional PMSM rather than OW-PMSM. In [21], a two-target MPCC method is applied to reduce the torque ripple. Besides, it analyzes the limitation of the inverter. However, it requires large calculational efforts in choosing optimal factor in cost function. A novel three-vector predictive control strategy based on energy storage model for hybrid-inverter OW-PMSM system is proposed in [22]. The duty cycle can be obtained and current ripples can be suppressed in it. However, there is no ZSL in the system, so ZSC is not considered.

In OW-PMSM system with a common dc bus topology, the ZSC in ZSL can negatively affect the performance of the system, which should be suppressed effectively. In [23], the causes of ZSC have been analyzed and identified, but it concentrated on OW induction motor rather than OW-PMSM. In [24], the zero common-mode VV is selected to eliminate the ZSC for nine-phase OW-PMSM. Different from [23] and [24], the ZSL back-EMF is another main source of ZSC in three-phase OW-PMSM, so the methods in them are not suitable for three-phase OW-PMSM. Several VVs are applied to suppress ZSC and synthesize desired voltage in [25], but the calculational effort has increased by varying remaining times of vectors. In [26], a quadrature-signal generator that generates a 90°-lagging signal is applied to generate the zero-sequence voltage (ZSV) reference, but the parameters should be found according to a large table, increasing the complexity of the system. In [27], ZSC in three-phase OW-PMSM system with a common dc bus is systematically analyzed, and a mathematical model of equivalent zero-sequence circuit considering parasitic effects of switching devices and the cross-coupling voltages is proposed. A cost function which contains ZSC is defined in [28] and [29], and Yuan et al. [29] can avoid the deterioration of ZSC in the case of ZSL parameter mismatch, but unsatisfactory ZSC and torque ripples still exist in these articles. Therefore, in FCS–MPCC in OW-PMSM with a common dc bus topology, ZSC suppression should be taken seriously. However, not adequate research has been focused on it.

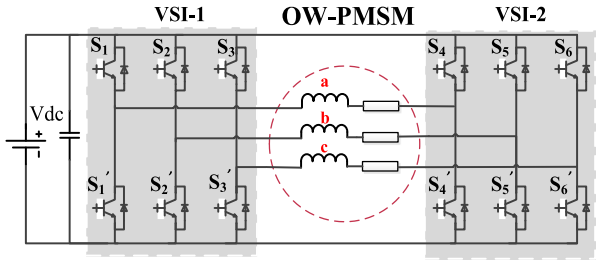

Fig. 1. Topology of OW-PMSM system with a common DC bus.

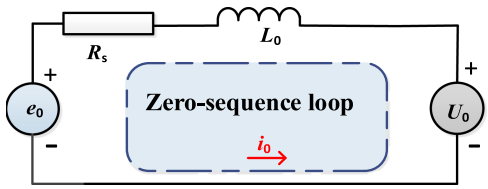

Fig. 2. Zero-sequence loop in OW-PMSM with common DC bus.

From all abovementioned papers, we can find that there are not many control methods that can address the calculational effort, reduce current and torque ripples, and suppress ZSC simultaneously for OW-PMSM with a common dc bus topology.

In order to relieve the computational burden, reduce the current and torque ripples, and suppress the ZSC for OW-PMSM with a common dc bus, in this article, a novel FCS–MPC method, termed HFCS–MPCC–DB, is proposed. The most significant contributions can be summarized as follows:

1) Considering DB principle and sector distribution strategy, a cost function is defined to reduce the computation time of FCS–MPCC. In the cost function, ZSV is overlooked and then considered separately. The number of feasible VVs is only 5, which reduces a lot computation time.
2) Based on (1), to make the system have a better performance, another novel cost function is defined to obtain the optimal ratio duty of one of two voltage-source inverters (VSIs) system, and the ZSC, the current, and torque ripples have been suppressed effectively. The effectiveness of the proposed method is validated based on several simulation and experiments results.

The rest of this article is organized as follows. Section II presents the mathematic model of OW-PMSM with a common dc bus. Sections III and IV, respectively, illustrate traditional FCS–MPCC and proposed HFCS–MPCC–DB. In Sections V and VI, the results of the simulation and experiments are shown, respectively. Finally, Section VII concludes this article.

II. OW-PMSM System With Common DC Bus

A. Topology of OW-PMSM System With Common DC Bus

The topology of OW-PMSM system with a common dc bus is presented in Fig. 1. There are two VSI systems and one power supply. The inherent ZSL is shown in Fig. 2.

B. Mathematical Model of OW-PMSM

In order to reduce the times of coordinate conversions, the mathematical model of OW-PMSM equations in $\alpha\beta0$ stationary frame can be described as

$$\begin{cases} U_\alpha = R_s i_\alpha + L_s \dfrac{di_\alpha}{dt} - \omega_r \psi_f \sin(\theta) \\ U_\beta = R_s i_\beta + L_s \dfrac{di_\beta}{dt} + \omega_r \psi_f \cos(\theta) \\ U_0 = R_s i_0 + L_0 \dfrac{di_0}{dt} + e_0 \end{cases} \tag{1}$$

$$\begin{cases} U_0 = \dfrac{1}{3}(U_a + U_b + U_c) \\ i_0 = \dfrac{1}{3}(i_a + i_b + i_c) \end{cases} \tag{2}$$

$$T_e = 1.5p * \left(\psi_f i_s + \frac{2e_0 i_0}{\omega_r}\right) \tag{3}$$

where U_α, U_β, and U_0 represent voltages of α-axis, β-axis, and ZSL, respectively; i_α, i_β, and i_0 stand for currents of α-axis, β-axis, and ZSL, respectively; L_s, R_s, Ψ_f, θ, L_0, p, ω_r, and e_0, denote the stator inductance, stator resistance, fundamental rotor flux-linkage, electrical rotor position, ZSL inductance, the number of pole pairs, electrical rotor angular speed, and zero-sequence back EMF, respectively; U_0 and i_0 can be obtained by (2), and U_a, U_b, U_c, i_a, i_b, and i_c are the phase voltages and phase currents, respectively. The torque model can be expressed as (3). Since the third harmonic is the main content of e_0, e_0 can be expressed as (4), where Ψ_{3f} is ZSL flux-linkage [24]

$$e_0 \approx -3\omega_r \psi_{3f} \sin(3\theta). \tag{4}$$

III. Traditional Finite Control Set Model Predictive Current Control

In traditional FCS–MPCC, the best VV is selected by minimizing a cost function among all feasible vectors. According to the first-order forward Euler discretization, one-step current prediction is presented as

$$\begin{aligned} \hat{i}_\alpha(k+1) &= \frac{T_k}{L_s}\left(U_\alpha(k) - R_s i_\alpha(k) \right. \\ &\quad \left. + \omega_r(k)\psi_f \sin(\theta(k))\right) + i_\alpha(k) \\ \hat{i}_\beta(k+1) &= \frac{T_k}{L_s}\left(U_\beta(k) - R_s i_\beta(k) \right. \\ &\quad \left. - \omega_r(k)\psi_f \cos(\theta(k))\right) + i_\beta(k) \\ \hat{i}_0(k+1) &= \frac{T_s}{L_0}\left(U_0(k) - R_s i_0(k) \right. \\ &\quad \left. + 3\psi_{3f}\omega_r(k)\sin(3\theta(k))\right) + i_0(k) \end{aligned} \tag{5}$$

where $\hat{i}_\alpha(k+1)$,$\hat{i}_\beta(k+1)$, and $\hat{i}_o(k+1)$ denote the estimations of the $(k+1)$th instant α-axis current, β-axis current, and ZSC, respectively. $U_\alpha(k)$, $U_\beta(k)$, $i_\alpha(k)$, and $i_\beta(k)$ represent the selected VV and measured current in α-axis and β-axis at kth instant, respectively. We assume that $\omega_r(k)\approx\omega_r(k+1)$, $\theta(k)\approx\theta(k+1)$, and apply the delay compensation method in [30], then $(k+2)$th instant current can be described as

$$\begin{aligned} \hat{i}_{\alpha i}(k+2) &= \frac{T_k}{L_s}\left(U_\alpha(i) - R_s\hat{i}_\alpha(k+1) \right. \\ &\quad \left. + \omega_r(k)\psi_f \sin(\theta(k))\right) + \hat{i}_\alpha(k+1) \\ \hat{i}_{\beta i}(k+2) &= \frac{T_k}{L_s}\left(U_\beta(i) - R_s\hat{i}_\beta(k+1) \right. \\ &\quad \left. - \omega_r(k)\psi_f \cos(\theta(k))\right) + \hat{i}_\beta(k+1) \\ \hat{i}_{0i}(k+2) &= \frac{T_s}{L_0}\left(U_0(i) - R_s\hat{i}_0(k+1) \right. \\ &\quad \left. + 3\psi_{3f}\omega_r(k)\sin(3\theta(k))\right) + \hat{i}_0(k+1) \end{aligned} \tag{6}$$

where $i = 1, 2, \ldots, 26, 27$ represents the available VVs in VSI system. Based on the principle that the least upper bridge arm switching state is turned ON and overlook the redundant VVs, 27 vectors are presented in Table I and shown in Fig. 3. U_0 represents inherent ZSV of the switching state and can be calculated by (7), where V_{dc} is the dc voltage and S_i (i = 1,2…5,6) is the switching state of upper bridge arm in Fig. 1. "1" means the upper bridge is turned ON and "0" means turned OFF

$$U_0 = \frac{1}{3}((S_1 - S_4) + (S_2 - S_5) + (S_3 - S_6)) \times V_{dc}. \tag{7}$$

For a simplified representation, use 0, 1, 2, 3, 4, 5, 6, and 7 to denote the switching state (000), (100), (110), (010), (011), (001), (101), and (111), respectively. i and j' (i, j = 0, 1, …6, 7) denote the switching state of VSI-1 and VSI-2, respectively.

TABLE I
Voltage Vectors of OW-PMSM With Common DC Bus

Vector number	Switching state (S_1, S_2, S_3—S_4, S_5, S_6)	U_α	U_β	U_0
1	(1—0')	2/3 U_{dc}	0	1/3 U_{dc}
2	(0—4')	2/3 U_{dc}	0	−2/3 U_{dc}
3	(1—4')	4/3 U_{dc}	0	−1/3 U_{dc}
4	(1—5')	U_{dc}	$\sqrt{3}$/3 U_{dc}	0
5	(2—0')	1/3 U_{dc}	$\sqrt{3}$/3 U_{dc}	2/3 U_{dc}
6	(0—5')	1/3 U_{dc}	$\sqrt{3}$/3 U_{dc}	−1/3 U_{dc}
7	(2—5')	2/3 U_{dc}	2$\sqrt{3}$/3 U_{dc}	1/3 U_{dc}
8	(3—5')	0	2$\sqrt{3}$/3 U_{dc}	0
9	(3—0')	−1/3 U_{dc}	$\sqrt{3}$/3 U_{dc}	1/3 U_{dc}
10	(0—6')	−1/3 U_{dc}	$\sqrt{3}$/3 U_{dc}	−2/3 U_{dc}
11	(3—6')	−2/3 U_{dc}	2$\sqrt{3}$/3 U_{dc}	−1/3 U_{dc}
12	(3—1')	− U_{dc}	$\sqrt{3}$/3 U_{dc}	0
13	(4—0')	−2/3 U_{dc}	0	2/3 U_{dc}
14	(0—1')	−2/3 U_{dc}	0	−1/3 U_{dc}
15	(4—1')	−4/3 U_{dc}	0	1/3 U_{dc}
16	(5—1')	− U_{dc}	−$\sqrt{3}$/3 U_{dc}	0
17	(5—0')	−1/3 U_{dc}	−$\sqrt{3}$/3 U_{dc}	1/3 U_{dc}
18	(0—2')	−1/3 U_{dc}	−$\sqrt{3}$/3 U_{dc}	−2/3 U_{dc}
19	(5—2')	−2/3 U_{dc}	−2$\sqrt{3}$/3 U_{dc}	−1/3 U_{dc}
20	(5—3')	0	−2$\sqrt{3}$/3 U_{dc}	0
21	(6—0')	1/3 U_{dc}	−$\sqrt{3}$/3 U_{dc}	2/3 U_{dc}
22	(0—3')	1/3 U_{dc}	−$\sqrt{3}$/3 U_{dc}	−1/3 U_{dc}
23	(6—3')	2/3 U_{dc}	−2$\sqrt{3}$/3 U_{dc}	1/3 U_{dc}
24	(1—3')	U_{dc}	$\sqrt{3}$/3 U_{dc}	0
25	(0—0')	0	0	0
26	(7—0')	0	0	U_{dc}
27	(0—7')	0	0	− U_{dc}

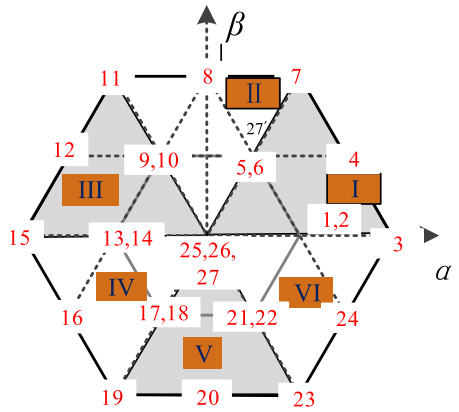

Fig. 3. Twenty-seven voltage vectors in the system.

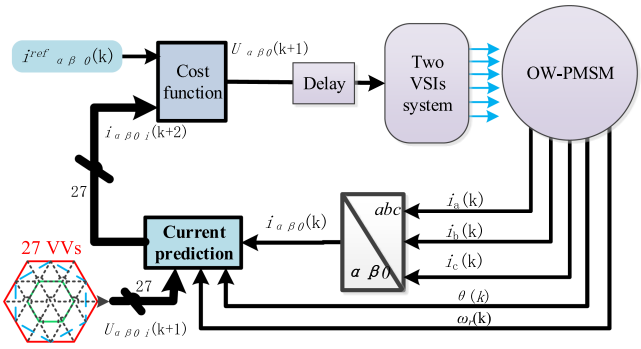

Fig. 4. Diagram of traditional FCS–MPCC.

For example, (2-3') represents switching state 2(110) in VSI-1 and 3'(010) in VSI-2.

The cost function is defined as follows [29]:

$$g(i)=\begin{cases}\left|i_{\alpha}^{\mathrm{ref}}(\mathrm{k})-\hat{i}_{\alpha i}(k+2)\right|+\left|i_{\beta}^{\mathrm{ref}}(\mathrm{k})-\hat{i}_{\beta i}(k+2)\right| \\ +\left|i_{0}^{\mathrm{ref}}(k)-\hat{i}_{0 i}(k+2)\right|\end{cases} \tag{8}$$

where $g(i)$ is the value of cost function, ${i_\alpha}^{\mathrm{ref}}$, ${i_\beta}^{\mathrm{ref}}$, and ${i_0}^{\mathrm{ref}}$ are the current references in α-axis, β-axis, and ZSL, respectively. According to the principle of minimizing cost function, the optimal VV could be selected. The diagram of traditional FCS–MPCC is shown in Fig. 4. It is clear that there are 27 candidate VVs that need to be calculated in the $(k+2)$th current prediction and cost function, which has a large computational burden.

IV. Proposed Finite Set Model Predictive Current Control Based on Deadbeat Principle

In this section, to reduce the computational burden in traditional FCS–MPCC, an improved voltage selection strategy, which combines FCS–MPCC and the principle of DB control, is proposed in Section IV-A. After that, to solve the current ripples and suppress ZSC, half-FCS model predictive current control (HFCS–MPCC–DB) is proposed in Section VI-B. Besides, the theoretical analysis is also presented in Section VI-B.

TABLE II
Sector Information of Desired Voltages

S_e	1	2	3	4	5	6
Sector	I	III	II	V	VI	IV

A. Improved Voltage Selection Strategy

First, as (9), the desired voltage is calculated according to the principle of DB control [17]

$$\begin{aligned}U_{\alpha}^{\mathrm{ref}}(k+1)&=\frac{L_s}{T_k}\left(i_{\alpha}^{\mathrm{ref}}(k)-\hat{i}_{\alpha}(k+1)\right)\\&\quad+R_s\hat{i}_{\alpha}(k+1)-\omega_r(k)\psi_f\sin(\theta(k))\\U_{\beta}^{\mathrm{ref}}(k+1)&=\frac{L_s}{T_k}\left(i_{\beta}^{\mathrm{ref}}(k)-\hat{i}_{\beta}(k+1)\right)\\&\quad+R_s\hat{i}_{\beta}(k+1)+\omega_r(k)\psi_f\cos(\theta(k))\\U_{0}^{\mathrm{ref}}(k+1)&=\frac{L_0}{T_s}\left(i_{0}^{\mathrm{ref}}(k)-\hat{i}_{0}(k+1)\right)\\&\quad+R_s\hat{i}_{0}(k+1)-3\omega_r(k)\psi_{3f}\sin(3\theta(k))\end{aligned} \tag{9}$$

where $\hat{i}_{\alpha}(k+1)$,$\hat{i}_{\beta}(k+1)$, and $\hat{i}_{o}(k+1)$ are the same as those in (5). ${U_\alpha}^{\mathrm{ref}}(k+1)$, ${U_\beta}^{\mathrm{ref}}(k+1)$, and ${U_0}^{\mathrm{ref}}(k+1)$ are $(k+1)$th instant desired voltages in α-axis, β-axis, and ZSL, respectively.

As shown in Fig. 3, the entire VVs region is divided into six sectors by blue line, namely I, II, III, IV, V, and VI. The phase information of desired voltages is presented in (10). It has to be mentioned that ${U_s}^{\mathrm{ref}}={U_\alpha}^{\mathrm{ref}}+j\times{U_\beta}^{\mathrm{ref}}$

$$\theta^{\mathrm{DB}}=\tan^{-1}\left(\frac{U_{\beta}(k+1)}{U_{\alpha}(k+1)}\right). \tag{10}$$

To avoid calculating the θ^{DB} using (10) in the hardware and reduce the number of possible VVs, the selection method, as shown in (11), (12), and Table II, is applied to get the sector information of the desired voltages in this article

$$\begin{cases}V_a=U_{\alpha}(k+1)\\V_b=\dfrac{\sqrt{3}}{2}U_{\beta}(k+1)-\dfrac{1}{2}U_{\alpha}(k+1)\\V_c=-\dfrac{\sqrt{3}}{2}U_{\beta}(k+1)-\dfrac{1}{2}U_{\alpha}(k+1)\end{cases} \tag{11}$$

$$\begin{cases}Se=0;\\Se=Se+1;\quad(V_a>0)\\Se=Se+2;\quad(V_b>0)\\Se=Se+4;\quad(V_c>0).\end{cases} \tag{12}$$

After getting the sector information, the cost function is defined as

$$\begin{aligned}g(i)=&\left|U_{\alpha}^{\mathrm{ref}}(k+1)-U_{\alpha i}\right|\\&+\left|U_{\beta}^{\mathrm{ref}}(k+1)-Ui_{\beta i}\right|+\left|U_{0}^{\mathrm{ref}}(k)-U_{0i}\right|\end{aligned} \tag{13}$$

where $i=1,2\ldots7,8$ denotes the VVs adjacent to the desired voltage. As shown in Fig. 5, there are only five active VVs and

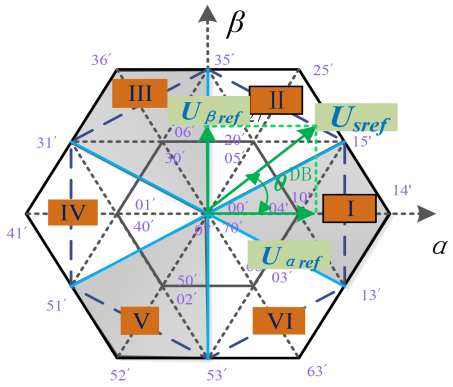

Fig. 5. Voltage vectors selection principle.

TABLE III
SWITCHING STATE IN SECTOR I

Sector	Vector number	U_α	U_β	Switching state (S_1, S_2, S_3– S_4, S_5, S_6)
I	18	U_{dc}	$-\sqrt{3}/3\ U_{dc}$	(1–3')
	1	$2/3\ U_{dc}$	0	U_0^{ref}>–n, (1–0')
				U_0^{ref}<–n, (0–4')
	2	$4/3\ U_{dc}$	0	(1–4')
	3	U_{dc}	$\sqrt{3}/3\ U_{dc}$	(1–5')
	19	0	0	U_0^{ref}>m, (7–0')
				U_0^{ref}<– m, (0–7')
				$\lvert U_0^{ref}\rvert$<m, (0–0')

three zero VVs need to be considered in one sector. For example, when U_s^{ref} is located in Sector II, V_4(1–5'), V_5 (0–5'), V_6 (2–0'), V_7 (2–5'), V_8 (3–5'), V_{25} (0–0'), V_{26} (7–0'), and V_{27} (0–7') are considered as candidate vectors. Compared to traditional FCS–MPCC, it can reduce calculational burden effectively. In order to further reduce the amount of calculation, $g(i)$ can be defined as

$$g(i) = \left|U_\alpha^{ref}(k{+}1) - U_{\alpha i}\right| + \left|U_\beta^{ref}(k{+}1) - Ui_{\beta i}\right| \qquad (14)$$

where $i = 1, 2 \ldots 4, 5$. In (14), ZSV part is overlooked. The optimal voltage which only considers α-β voltage is selected. Then, redundant vector is applied reasonably to address the ZSV. The number of candidate VVs is reduced from 8 to 5 and $g(i)$ is simpler than that in (13). However, not all VVs has redundant vector. The VVs selection principle in sector I is presented in Table III, where $n = \frac{1}{6}\ U_{dc}$ and $m = \frac{1}{2}\ U_{dc}$, respectively, presents the midpoint of possible ZSV of the redundant vectors. The VV selection principle in other sectors is the same as it. Then, the selected vector can be implied in the control system directly. We name this selection principle as improved FCS–MPCC based on DB (IFCS–MPCC–DB).

B. Half-Finite Control Set Model Predictive Current Control Based on Deadbeat Principle

IFCS–MPCC–DB has reduced the computational burden of FCS–MPCC effectively. However, large current and torque ripples, and bad ZSC performance still exist in the system. To address the aforementioned problems, in this part, HFCS–MPCC–DB is proposed. After selecting optimal VV by (14), the switching state of one side of VSI is fixed and the other side is adjusted to suppress the ZSC and current ripples. In order to have a maximum adjustment range, the number of upper bridge arms should be turned OFF as much as possible. The VV candidates are presented in Table IV. We still use Sector I as an example, which is shown in Fig. 6.

TABLE IV
CANDIDATE VVS IN HFCS–MPCC–DB

Sector	Vector number	Switching state (a-b')	U_α	U_β	U_0^i
I	18	(1–3')	U_{dc}	$-\sqrt{3}/3\ U_{dc}$	0
	1	(1–0')	$2/3\ U_{dc}$	0	$1/3\ U_{dc}$
	2	(1–4')	$4/3\ U_{dc}$	0	$-1/3\ U_{dc}$
	3	(1–5')	U_{dc}	$\sqrt{3}/3\ U_{dc}$	0
	19	(0–0')	0	0	0
II	3	(1–5')	U_{dc}	$\sqrt{3}/3\ U_{dc}$	0
	4	(0–5')	$1/3\ U_{dc}$	$\sqrt{3}/3\ U_{dc}$	$-1/3\ U_{dc}$
	5	(2–5')	$2/3\ U_{dc}$	$2\sqrt{3}/3\ U_{dc}$	$1/3\ U_{dc}$
	6	(3–5')	0	$2\sqrt{3}/3\ U_{dc}$	0
	19	(0–0')	0	0	0
III	6	(3–5')	0	$2\sqrt{3}/3\ U_{dc}$	0
	7	(3–0')	$-1/3\ U_{dc}$	$\sqrt{3}/3\ U_{dc}$	$1/3\ U_{dc}$
	8	(3–6')	$-2/3\ U_{dc}$	$2\sqrt{3}/3\ U_{dc}$	$-1/3\ U_{dc}$
	9	(3–1')	$-\ U_{dc}$	$\sqrt{3}/3\ U_{dc}$	0
	19	(0–0')	0	0	0
IV	9	(3–1')	$-U_{dc}$	$\sqrt{3}/3\ U_{dc}$	0
	10	(0–1')	$-2/3\ U_{dc}$	0	$-1/3\ U_{dc}$
	11	(4–1')	$-4/3\ U_{dc}$	0	$1/3\ U_{dc}$
	12	(5–1')	$-U_{dc}$	$-\sqrt{3}/3\ U_{dc}$	0
	19	(0–0')	0	0	0
V	12	(5–1')	$-U_{dc}$	$-\sqrt{3}/3\ U_{dc}$	0
	13	(5 -0')	$-1/3\ U_{dc}$	$-\sqrt{3}/3\ U_{dc}$	$1/3\ U_{dc}$
	14	(5–2')	$-2/3\ U_{dc}$	$-2\sqrt{3}/3\ U_{dc}$	$-1/3\ U_{dc}$
	15	(5–3')	0	$-2\sqrt{3}/3\ U_{dc}$	0
	19	(0–0')	0	0	0
VI	15	(5–3')	0	$-2\sqrt{3}/3\ U_{dc}$	0
	16	(0–3')	$1/3\ U_{dc}$	$-\sqrt{3}/3\ U_{dc}$	$-1/3\ U_{dc}$
	17	(6–3')	$2/3\ U_{dc}$	$-2\sqrt{3}/3\ U_{dc}$	$1/3\ U_{dc}$
	18	(1–3')	U_{dc}	$-\sqrt{3}/3\ U_{dc}$	0
	19	(0–0')	0	0	0

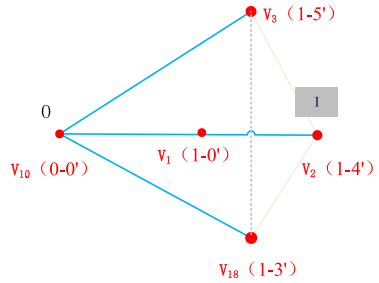

Fig. 6. Candidate VVs in sector I.

The selected VV has an inherent ZSV, which is denoted as $U_0{}^i$ in Table IV. Comparing the inherent ZSV and $U_0{}^{ref}$ to determine which VSI's switching state should be fixed and by contrast, switching state of the other VSI should be adjusted. More specifically, if inherent ZSV $U_0{}^i > U_0{}^{ref}(k{+}1)$, the switching state of VSI-1 is fixed, and one zero vector "7"(111) and selected vector are applied in VSI-2. When $U_0{}^i < U_0{}^{ref}(k{+}1)$, the switching

state of VSI-2 is fixed, and the zero-vector "7"(111) and selected vector are applied in VSI-1.

We introduce the variables $U_{f\alpha}$, $U_{f\beta}$, $U_{a\alpha}$, and $U_{a\beta}$ to denote the voltage in α-β frame that fixed VSI system and the adjusted VSI system can be produced by selected VV, respectively. For example, if the selected VV is *a-b*' (S_1 S_2 S_3–S_4 S_5 S_6) and inherent ZSV is ${U_0}^i$. When ${U_0}^i > {U_0}^{\text{ref}}(k+1)$, the switching state of VSI-1 is fixed, and the switching state of VSI-2 needs to be adjusted (($S_4S_5S_6$) + (111)). The distribution factor x_t is defined as

$$x_t = \frac{T_{(111)}}{T_s} \tag{15}$$

where $T_{(111)}$ denotes the effective time ratio of zero voltage (111) in VSI-2. Then, effective duration ratio of b' is $(1 - x_t)$. $h(x_t)$ is defined as

$$\begin{aligned} h(x_t) &= \left|\left(U_\alpha\,(k+1) - U_{f\alpha}\right) - (1-x_t)\,U_{a\alpha}\right|^2 \\ &\quad + \left|\left(U_\beta\,(k+1) - U_{f\beta}\right) - (1-x_t)\,U_{a\beta}\right|^2 \\ &\quad + \left|U_0\,(k+1) - (1-x_t)\,U_0^i - \alpha x_t\right|^2 \\ &= Ax_t + Bx_t^2 \end{aligned} \tag{16}$$

$$A = \left\{ \begin{array}{l} \left(U_\alpha^{\text{ref}}\,(k+1) - U_{f\alpha}\right)U_{a\alpha} - U_{a\alpha}^2 \\ \quad + \left(U_\beta^{\text{ref}}\,(k+1) - U_{f\beta}\right)U_{a\beta} - U_{a\beta}^2 + \alpha U_0^i \\ -\left(U_0^i\right)^2 - \alpha U_0^{\text{ref}}\,(k+1) + U_0^i U_0^{\text{ref}}\,(k+1) \end{array} \right\}$$

$$B = \left(U_{a\alpha}^2 + U_{a\beta}^2 + \alpha^2 - 2\alpha U_0^i + \left(U_0^i\right)^2\right) \tag{17}$$

where α denotes the ZSV when switching state of adjusted VSI is (111). To ensure that $h(x_t)$ has a minimum value, a reasonable x_t must be obtained, which means following equations should be satisfied:

$$\frac{\partial h}{\partial x_t} = A + Bx_t \tag{18}$$

$$\left\{ \begin{array}{l} \frac{\partial h}{\partial x_t} = 0 \quad \Rightarrow x_{\text{t}} = -\frac{A}{B} \quad (B \neq 0) \quad (0 \le x_t \le 1) \\ x_t = 0 \quad (B = 0 \quad and \quad A \ge 0) \\ x_t = 1 \quad (B = 0 \quad and \quad A < 0)\,. \end{array} \right. \tag{19}$$

After obtaining x_t, the durations of S_1, S_2, S_3, S_4, S_5, and S_6 can be expressed as (20).

For example, if the selected VV is 1–5'(100–001), the inherent ZSV is 0 (${U_0}^i = 0U_{\text{dc}}$). We assume that $0 > {U_0}^{\text{ref}}(k+1)$, then the switching state of VSI-1 is fixed (100) and VSI-2 should be adjusted (001+111). Equations (21)–(23) can be obtained based on (17)–(20)

$$\left\{ \begin{array}{ll} T_{s_1\text{on}} = S_1 \times T_s & \\ T_{s_2\text{on}} = S_2 \times T_s & \\ T_{s_3\text{on}} = S_3 \times T_s & \\ T_{s_4\text{on}} = (S_4 + x_t) \times T_s & (0 \le T_{s_4\text{on}} \le 1) \\ T_{s_5\text{on}} = (S_5 + x_t) \times T_s & (0 \le T_{s_5\text{on}} \le 1) \\ T_{s_6\text{on}} = (S_6 + x_t) \times T_s & (0 \le T_{s_6\text{on}} \le 1) \end{array} \right. \tag{20}$$

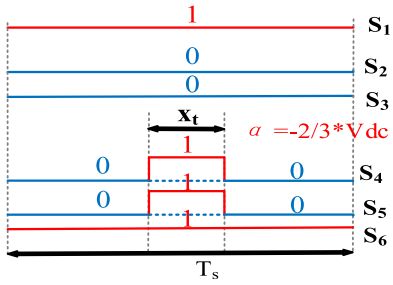

Fig. 7. Durations of S_1, S_2, S_3, S_4, S_5, and S_6.

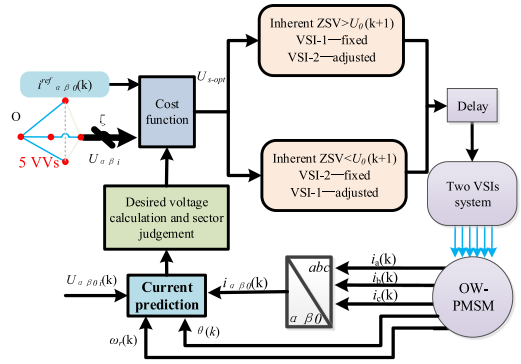

Fig. 8. Control block diagram of HFCS–MPCC–DB.

$$\left\{ \begin{array}{l} U_{f\alpha} = \frac{2}{3}U_{\text{dc}} \\ U_{f\beta} = 0 \\ U_{a\alpha} = \frac{1}{3}U_{\text{dc}} \\ U_{a\beta} = \frac{\sqrt{3}}{3}U_{\text{dc}} \end{array} \right. \tag{21}$$

$$\left\{ \begin{array}{l} \alpha = -\frac{2}{3}U_{\text{dc}} \\ x_t = -\frac{A}{B} \quad (0 \le x_t \le 1) \end{array} \right. \tag{22}$$

$$\left\{ \begin{array}{l} T_{s_1\text{on}} = T_s \\ T_{s_2\text{on}} = 0 \\ T_{s_3\text{on}} = 0 \\ T_{s4\text{on}} = x_t \times T_s \\ T_{s5\text{on}} = x_t \times T_s \\ T_{s6\text{on}} = T_s. \end{array} \right. \tag{23}$$

The durations of S_1, S_2, S_3, S_4, S_5, and S_6 is shown in Fig. 7. The control block diagram and flow chart of HFCS–MPCC–DB are, respectively, presented in Figs. 8 and 9.

We can find that in one control period, one active VV and a half zero VV (111) are applied. The optimal duty cycle of the vector (111) is obtained from the proposed novel cost function. By adjusting one of two VSIs, (111) can compensate the desired ZSV and as a result, and the ZSC can be suppressed and the currents ripples can be reduced effectively.

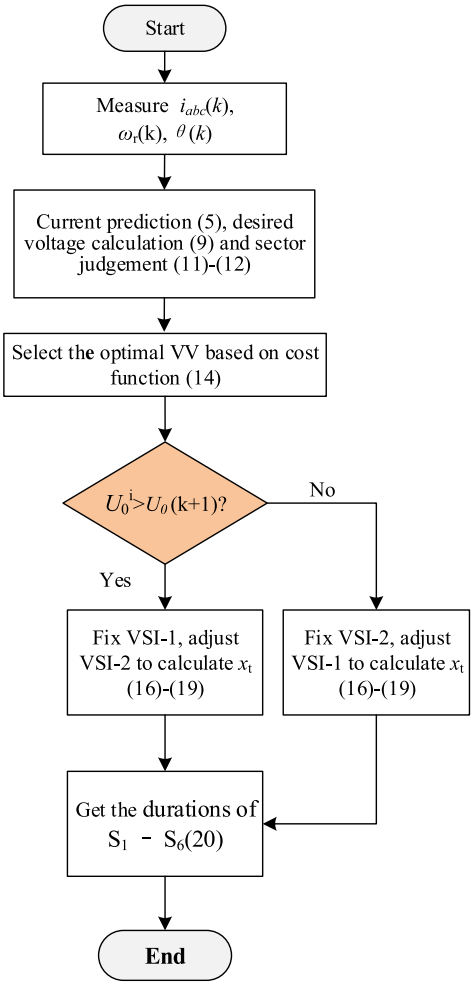

Fig. 9. Flow chart of HFCS–MPCC–DB.

TABLE V
OW-PMSM PARAMETERS

Parameter	Description	Value
P	Number of pole pairs	4
R_S	Stator resistance (Ω)	1.38
L_S	Stator inductance (mH)	3.21
L_0	Zero-sequence inductance (mH)	1.83
Ψ_{3f}	Rotor third harmonic flux linkage (Wb)	0.008
Ψ_f	Rotor flux linkage (Wb)	0.1667
T_N	Rated torque (Nm)	4
J	Rotational inertia (kg • m^2)	0.00085

V. SIMULATION STUDY

To validate the effectiveness of the proposed method, simulation has been done by MATLAB/Simulink. In this part, we present simulation results of three methods, respectively, namely traditional FCS–MPCC control method in [29] (denoted as Method 1), the IFCS–MPCC–DB voltage selection method (denoted as Method 2), and HFCS–MPCC–DB, (denoted as Method 3). Table V presents OW-PMSM parameters. The control frequency is set to 20 kHz, the dc voltage is set to 100 V, and the deadtime is set to 2.5 μs.

TABLE VI
SIMULATION RESULTS OF M_i AND J_i

	Method 1		Method 2		Method 3	
M/J	$M_{id/iq/Te}$	$J_{id/iq/Te}$	$M_{id/iq/Te}$	$J_{id/iq/Te}$	$M_{id/iq/Te}$	$J_{id/iq/Te}$
d-axis	0.22	0.25	0.21	0.22	0.19	0.21
q-axis	0.26	0.32	0.26	0.27	0.18	0.20
T_e	0.28	0.34	0.26	0.32	0.15	0.19

The simulation performance of current and torque at 1000 r/min are, respectively, shown in Figs. 10 and 11. The load torque is changed suddenly from 2 to 3 N‘m, and three methods have good track performance. i_{dref}, i_{qref}, and T_{eref} represent the current references in d-axis, q-axis, and torque reference, respectively. From Fig. 10, by comparing (a), (b), and (c), Method 1 and Method 2 have larger phase current harmonics, while Method 3 has a better performance in i_a. It is clear that Method 3 performs much better in ZSC than that of Method 1 and Method 2 by comparing (d), (e), and (f). The ZSC of Method 2 has worse performance than that of Method 1, which because that in Method 2, the cost function overlooks ZSV to reduce the computation time. By contrast, the current ripples in d-axis and q-axis have reduced because it gives priority to U_α and U_β. From Fig. 11, we can find that torque of Method 3 performs better than that of Method 1 and Method 2. According to [31], in order to compare the performance of current and torque clearer, $M_{i/Te}$ and $J_{i//Te}$ are defined as (24) and (25). The results are presented in Table VI. It can be seen that the proposed control Method 3 is effective in reducing current ripples, suppressing ZSC and torque ripples. The effectiveness in reducing calculational burden is shown in Section VI

$$M_{i_{/T_e}} = \frac{1}{N}\sum_{k=1}^{N}\left|e_{i_{/T_e}}(k)\right| = \frac{1}{N}\sum_{k=1}^{N}\left|\left(i^{\text{ref}}/T_e^{\text{ref}}(k)\right) - \left(i/T_e(k)\right)\right| \tag{24}$$

$$J_{i_{/T_e}} = \sqrt{\frac{1}{N}\sum_{k=1}^{N}\left(\left(i^{\text{ref}}/T_e^{\text{ref}}(k)\right) - \left(i/T_e(k)\right)\right)^2}. \tag{25}$$

VI. EXPERIMENTAL RESULTS

The traditional FCS–MPCC (Method 1) [29], IFCS–MPCC–DB (Method 2), and the proposed control method HFCS–MPCC–DB (Method 3) are implemented on the OW-PMSM platform. The control frequency is set to 20 kHz. The platform is shown in Fig. 12. The three control methods are compared under different conditions.

A. Experimental Results of Computation Time

First, the computation time of three control methods using the Code Composer Studio 8.2.0 software is presented in Table VII. Method 2 has shorter computation time than that of Method 1 and Method 3. Especially compared to Method 1, calculation time has reduced by more than 48%. The computation time of

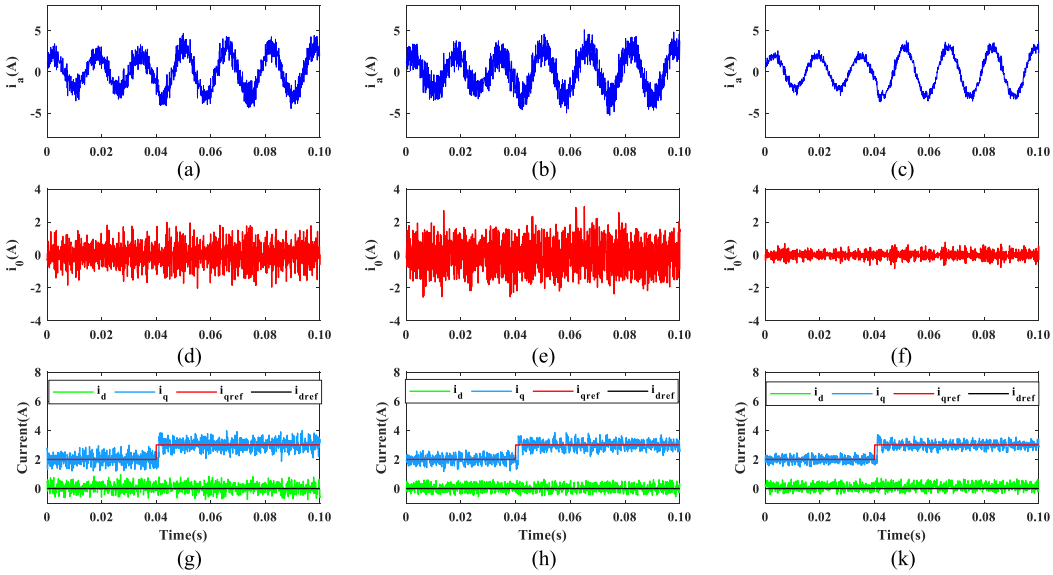

Fig. 10. Simulation results of phase current i_a, ZSC i_0, d-axis current i_d, q-axis current i_q at 1000 r/min. (a), (d), and (g) Method 1; (b), (e), and (h) Method 2; and (c), (f), and (k) Method 3.

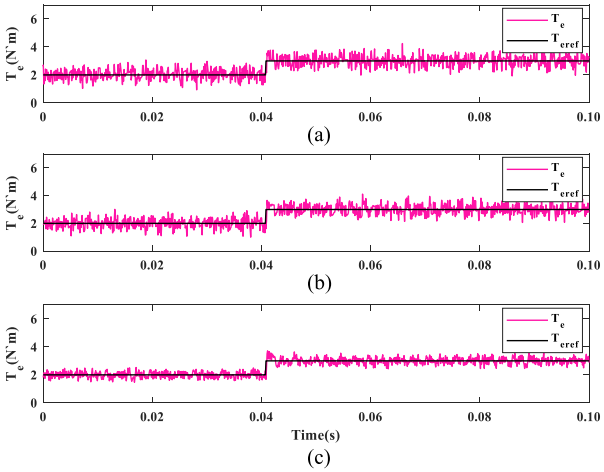

Fig. 11. Simulation results of torque at 1000 r/min. (a) Method 1; (b) Method 2; and (c) Method 3.

TABLE VII
COMPUTATION TIME OF THREE METHODS

Method	Method 1	Method 2	Method 3
Computation time	25.86 μs	13.33 μs	15.93 μs

Method 3 is a little longer than that of Method 2, while compared to Method 1, it is much shorter. This shows that the proposed control method can greatly reduce the calculational effort.

B. Experimental Results of Current Performance

Figs. 13–14 show the experimental results of the phase current i_a, ZSC i_0, d-axis current i_d, and q-axis i_q of OW-PMSM at 200 and 1300 r/min, respectively. In Fig. 13, the steady-state current performance is presented and the load torque is set to 2 N·m. By comparing the experimental results shown in (d), (e), and (f), it

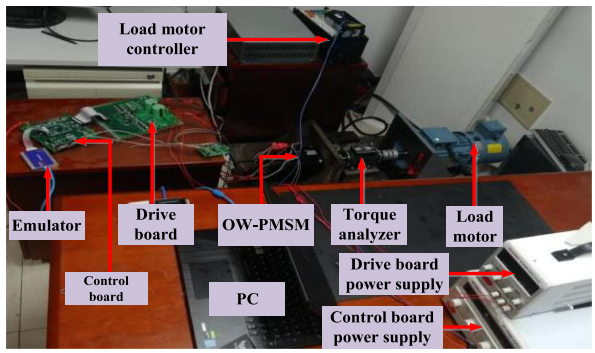

Fig. 12. Experimental platform of OW-PMSM system.

can be found that the HFCS–MPCC–DB method has the best performance in ZSC among the three control methods. And as a result, phase current performance of Method 3 is better than that in Method 1 and Method 2. Besides, to have a clearer comparison of phase currents, the experimental results of the total harmonic distortion (THD) are also presented in Fig. 13. It can be observed that Method 2 has the largest THD among the three methods, indicating its poor performance in ZSC suppression. On the other hand, Method 3 demonstrates the best THD performance, indicating its effectiveness in suppressing ZSC.

Fig. 14 shows the dynamic current performance and the load torque is changed from 2 to 5 N·m and then changed from 5 to 3 N·m. Evidently, among three methods, Method 3 performs best in ZSC and current ripples. The ZSC of Method 2 has worse performance than that of Method 1, but i_d and i_q performs better than Method 1. To have a comparison between the three methods in i_d and i_q ripples, M_i and J_i are also calculated, which is shown in Fig. 15. By comparing M_{id}, M_{iq}, J_{id}, and J_{iq} of these three methods, it can be seen that Method 3 is effective in suppressing the current ripples in d-axis and q-axis. Meanwhile,

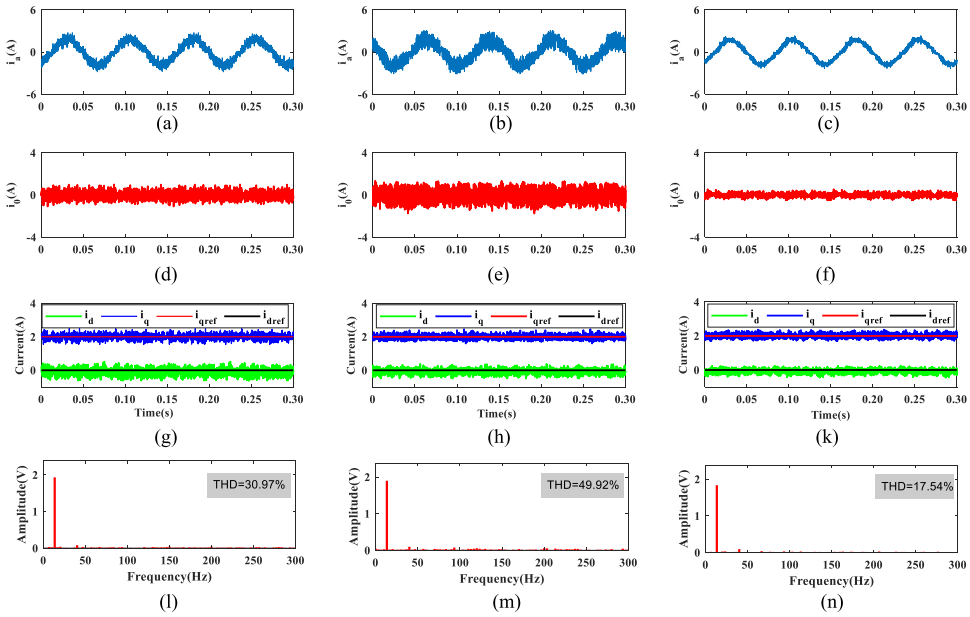

Fig. 13. Experimental steady-state performance at 200 r/min. (a), (d), (g), and (l) Phase current i_a, ZSC i_0, d-axis current i_d, q-axis i_q, and THD of Method 1. (b), (e), (h), and (m) Phase current i_a, ZSC i_0, d-axis current i_d, q-axis i_q, and THD of Method 2. (c), (f), (k), and (n) Phase current i_a, ZSC i_0, d-axis current i_d, q-axis i_q, and THD of Method 3.

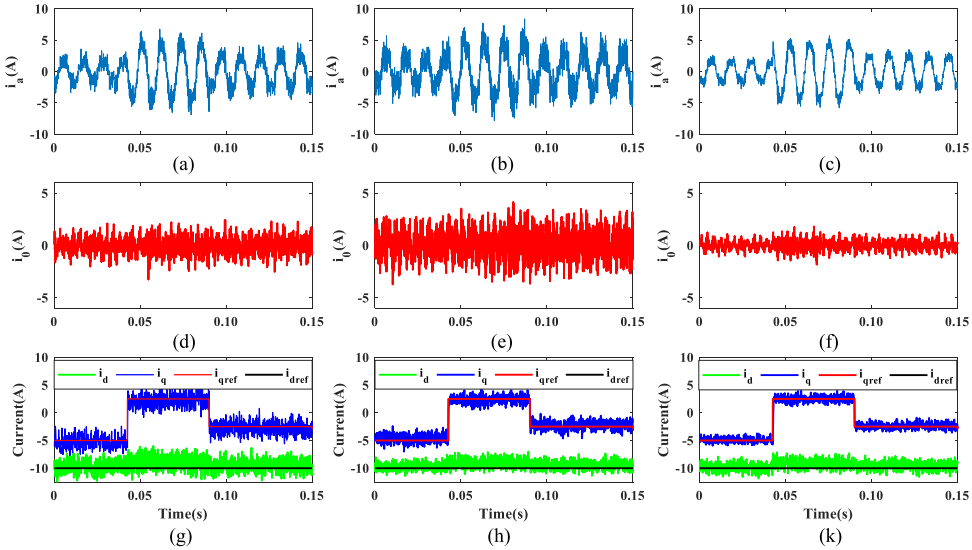

Fig. 14. Experimental dynamic performance at 1300 r/min. (a), (d), and (g) Phase current i_a, ZSC i_0, d-axis current i_d, and q-axis i_q of Method 1. (b), (e), and (h) Phase current i_a, ZSC i_0, d-axis current i_d, and q-axis i_q of Method 2. (c), (f), and (k) Phase current i_a, ZSC i_0, d-axis current i_d, and q-axis i_q of Method 3.

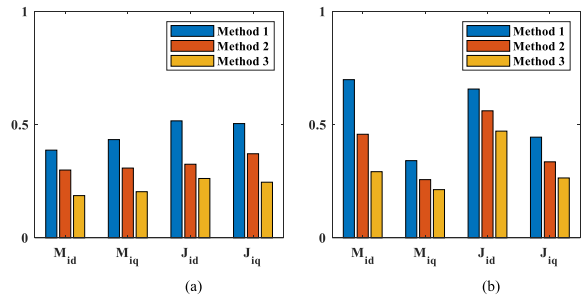

Fig. 15. Experimental result of M_{id}, M_{iq}, J_{id}, and J_{iq} of three methods. (a) 200 r/min. (b) 1300 r/min.

because Method 2 gives priority to U_α and U_β, it has worse ZSC performance than that of Method 1 but has lower current ripples in d-axis and q-axis.

In order to have a comparison with other methods, Fig. 16 presents the experimental results of phase current i_a, and ZSC i_0 of Method 1, Method 2, Method 3, and the control method in [18] (denoted as Method 4). The speed is set to 900 r/min and the load torque is set to 3 N‘m. We can find that phase current and ZSC of Method 3 performs better than other three methods. Moreover, the value of THD of Method 3 is smaller than those of Method 1, Method 2, and Method 4. Table VIII shows the comparison between the four methods. It has to be mentioned

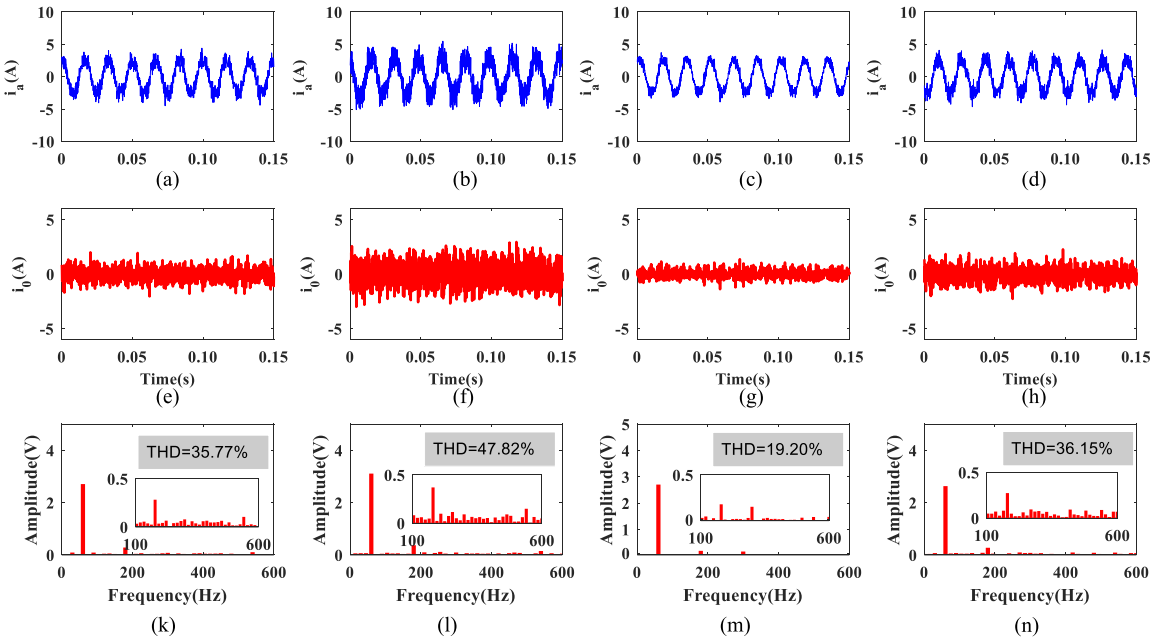

Fig. 16. Experimental results of different methods. (a), (e), and (k) Phase current i_a, ZSC i_0, and THD of phase current of Method 1. (b), (f), and (l) Phase current i_a, ZSC i_0, and THD of phase current of Method 2. (c), (g), and (m) Phase current i_a, ZSC i_0, and THD of phase current of Method 3. (d), (h), and (n) Phase current i_a, ZSC i_0, and THD of phase current of Method 4.

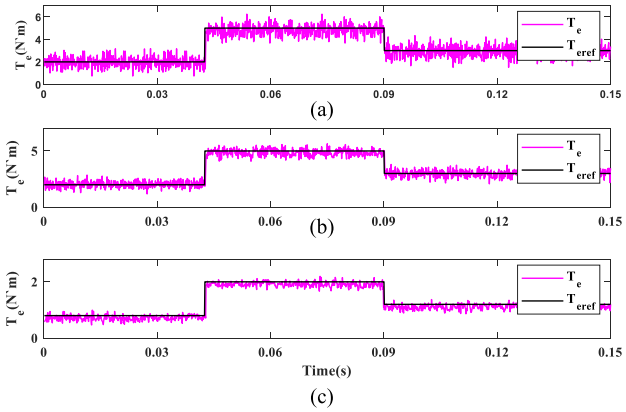

Fig. 17. Experimental results of torque at 1300 r/min. (a) Method 1. (b) Method 2. (c) Method 3.

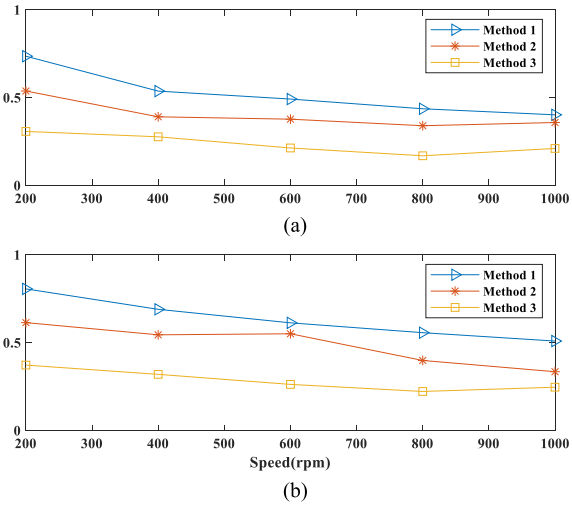

Fig. 18. Experimental results of M_{Te} and J_{Te} of three methods under different speed. (a) M_{Te}. (b) J_{Te}.

that Δi_0 is calculated by (26), and the sum of m and n is the total number of sampling points

$$\begin{cases} \Delta i_0 = i_0^{m+} - i_0^{m-} \\ i_0^{m+} = \dfrac{1}{m}\sum_{i=1}^{m} i_0(m) \qquad (i_0(m) > 0) \\ i_0^{m+} = \dfrac{1}{n}\sum_{i=1}^{n} i_0(n) \quad (i_0(n) < 0). \end{cases} \tag{26}$$

C. Experimental Results of Torque Performance

Figs. 17 and 18 show the experimental results of torque performance. In Fig. 17, the speed is set to 1300 r/min and the load torque is changed from 2 to 5 N·m and then changed from 5 to 3 N·m. Clearly, the torque of Method 3 performs much better than that of Method 1 and Method 2. To compare the torque performance under different condition, Fig. 18 presents the results of M_{Te} and J_{Te} of three methods. The load torque is set to 2 N·m. It can be seen that M_{Te} and J_{Te} almost have the same trend and Method 3 always has the best torque performance among three methods.

From above experimental results, we can deduce that the proposed Method 3 is effective in reducing calculation time, suppressing current and torque ripples, and suppressing ZSC, no matter at low or high speed, dynamic or steady state.

TABLE VIII
COMPARISON BETWEEN EXISTING METHODS AND PROPOSED METHOD

Item	Traditional FCS–MPCC [29]	IFCS–MPCC–DB	HFCS–MPCC–DB	The FCS–MPCC–DB [18]
Number of distributed sectors	Undistributed	6	6	24
Number of candidate voltage vectors	27	5	5	4-7
ZSC performance (Δi_0)	0.92	1.68	0.45	1.08
Phase current performance (THD)	35.77%	47.82%	19.20%	36.15%
Control parameter tuning	Unrequired	Unrequired	Unrequired	Required
Simplified control flow chart	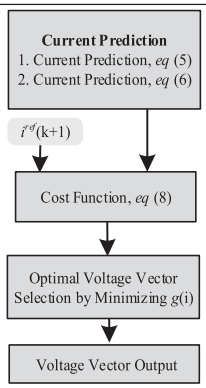	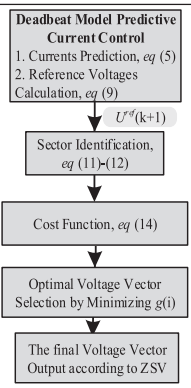	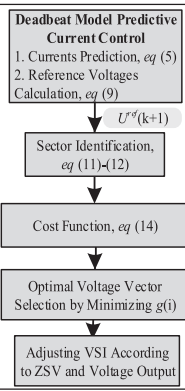	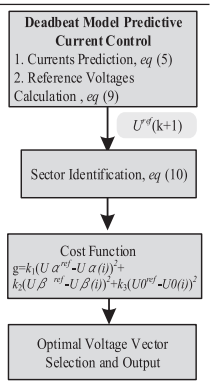

VII. CONCLUSION

To improve the performance of FCS–MPCC in OW-PMSM with a common dc bus, a novel control method, termed HFS–MPCC–DB, is proposed in this article. The main conclusions can be expressed as follows:

1) The proposed method can reduce the computation time compared to traditional FCS–MPCC. By combining the FCS–MPCC and the principle of DB, considering redundant VVs and reasonable sector distribution strategy, an optimized cost function has been defined to choose optimal VV, which can greatly reduce the computational effort.
2) After selecting optimal VV, the duty time of one of the two VSIs is adjusted and as a result, the ZSC, *d*-axis, and *q*-axis current ripples, and torque ripples have been suppressed effectively.
3) The comparative simulation and experimental studies have been conducted and the results have proved that the proposed HFCS–MPCC–DB method maintains better performance in phase current, ZSC, current, and torque ripples than those of traditional FCS–MPCC and FCS–MPCC–DB. Therefore, the proposed control method can be experimentally applied to OW-PMSMs drives.

REFERENCES

[1] J. Hang, J. Zhang, M. Xia, S. Ding, and W. Hua, "Interturn fault diagnosis for model-predictive-controlled-PMSM based on cost function and wavelet transform," *IEEE Trans. Power Electron.*, vol. 35, no. 6, pp. 6405–6418, Jun. 2020.

[2] W. Hu, C. Ruan, H. Nian, and D. Sun, "An improved modulation technique with minimum switching actions within one PWM cycle for open-end winding PMSM system with isolated DC bus," *IEEE Trans. Ind. Electron.*, vol. 67, no. 5, pp. 4259–4264, May 2020.

[3] Q. An, J. Liu, Z. Peng, L. Sun, and L. Sun, "Dual-space vector control of open-end winding permanent magnet synchronous motor drive fed by dual inverter," *IEEE Trans. Power Electron.*, vol. 31, no. 12, pp. 8329–8342, Dec. 2016.

[4] B. Venugopal Reddy, V. T. Somasekhar, and Y. Kalyan, "Decoupled space-vector PWM strategies for a four-level asymmetrical open-end winding induction motor drive with waveform symmetries," *IEEE Trans. Ind. Electron.*, vol. 58, no. 11, pp. 5130–5141, Nov. 2011.

[5] Z. Shen, D. Jiang, and L. Zhu, "A novel zero-sequence current elimination PWM scheme for an open-winding PMSM with common DC bus," *IEEE Trans. Power Electron.*, vol. 34, no. 12, pp. 12476–12490, Dec. 2019.

[6] W. Hu, H. Nian, and D. Sun, "Zero-sequence current suppression strategy with reduced switching frequency for open-end winding PMSM drives with common DC bus," *IEEE Trans. Ind. Electron.*, vol. 66, no. 10, pp. 7613–7623, Oct. 2019.

[7] E. Fuentes, C. A. Silva, and R. M. Kennel, "MPC implementation of a quasi-time-optimal speed control for a PMSM drive, with inner modulated-FS-MPC torque control," *IEEE Trans. Ind. Electron.*, vol. 63, no. 6, pp. 3897–3905, Jun. 2016.

[8] Z. Chen, C. Wu, D. Zhong, and C. Qiang, "Robust deadbeat predictive current control for PMSM drives based on single FPGA implementation," in *Proc. IEEE Int. Symp. Predictive Control Elect. Drives Power Electron.*, 2019, pp. 1–6.

[9] O. Sandre-Hernandez, J. Rangel-Magdaleno, and R. Morales-Caporal, "A comparison on finite-set model predictive torque control schemes for PMSMs," *IEEE Trans. Power Electron.*, vol. 33, no. 10, pp. 8838–8847, Oct. 2018.

[10] J. Hang, J. Zhang, M. Xia, S. Ding, and W. Hua, "Interturn fault diagnosis for model-predictive-controlled-PMSM based on cost function and wavelet transform," *IEEE Trans. Power Electron.*, vol. 35, no. 6, pp. 6405–6418, Jun. 2020.

[11] J. Zou, W. Xu, Y. Liu, and C. Mu, "Multistep model predictive control for permanent magnet synchronous machine," in *Proc. IEEE Appl. Power Electron. Conf. Expo.*, 2017, pp. 525–531.

[12] L. Tarisciotti, P. Zanchetta, A. Watson, S. Bifaretti, and J. C. Clare, "Modulated model predictive control for a seven-level cascaded h-bridge back-to-back converter," *IEEE Trans. Ind. Electron.*, vol. 61, no. 10, pp. 5375–5383, Oct. 2014.
[13] M. Siami, D. A. Khaburi, M. Rivera, and J. Rodríguez, "A computationally efficient lookup table based FCS-MPC for PMSM drives fed by matrix converters," *IEEE Trans. Ind. Electron.*, vol. 64, no. 10, pp. 7645–7654, Oct. 2017.
[14] C. Sun, D. Sun, Z. Zheng, and H. Nian, "Simplified model predictive control for dual inverter-fed open-winding permanent magnet synchronous motor," *IEEE Trans. Energy Convers.*, vol. 33, no. 4, pp. 1846–1854, Dec. 2018.
[15] B. Zhu, K. Rajashekara, and H. Kubo, "A novel predictive current control for open-end winding induction motor drive with reduced computation burden and enhanced zero sequence current suppression," in *Proc. IEEE Appl. Power Electron. Conf. Expo.*, 2017, pp. 552–557.
[16] W. Xie et al., "Finite-control-set model predictive torque control with a deadbeat solution for PMSM drives," *IEEE Trans. Ind. Electron.*, vol. 62, no. 9, pp. 5402–5410, Sep. 2015.
[17] M. S. R. Saeed, W. Song, B. Yu, and X. Wu, "Low-complexity deadbeat model predictive current control with duty ratio for five-phase PMSM drives," *IEEE Trans. Power Electron.*, vol. 35, no. 11, pp. 12085–12099, Nov. 2020.
[18] L. Rovere, A. Formentini, and P. Zanchetta, "Finite control set-model predictive control for the dual fed common DC-link open-end winding PMSM drive," in *Proc. IEEE Int. Elect. Mach. Drives Conf.*, 2019, pp. 2203–2209.
[19] Y. Zhang, D. Xu, J. Liu, S. Gao, and W. Xu, "Performance improvement of model-predictive current control of permanent magnet synchronous motor drives," *IEEE Trans. Ind. Appl.*, vol. 53, no. 4, pp. 3683–3695, Jul./Aug. 2017.
[20] S. Kang, J. Soh, and R. Kim, "Symmetrical three-vector-based model predictive control with deadbeat solution for IPMSM in rotating reference frame," *IEEE Trans. Ind. Electron.*, vol. 67, no. 1, pp. 159–168, Jan. 2020.
[21] S. Liu, C. Liu, Y. Huang, and H. Zhao, "Model predictive two-target current control for OW-PMSM," *IEEE Trans. Power Electron.*, vol. 36, no. 3, pp. 3224–3235, Mar. 2021.
[22] C. Sun, D. Sun, W. Chen, and H. Nian, "Improved model predictive control with new cost function for hybrid-inverter open-winding PMSM system based on energy storage model," *IEEE Trans. Power Electron.*, vol. 36, no. 9, pp. 10705–10715, Sep. 2021.
[23] A. Somani, R. K. Gupta, K. K. Mohapatra, and N. Mohan, "On the causes of circulating currents in PWM drives with open-end winding AC machines," *IEEE Trans. Ind. Electron.*, vol. 60, no. 9, pp. 3670–3678, Sep. 2013.
[24] H. Wang, X. Wu, X. Zheng, and X. Yuan, "virtual voltage vector based model predictive control for a nine-phase open-end winding PMSM with a common DC bus," *IEEE Trans. Ind. Electron.*, vol. 69, no. 6, pp. 5386–5397, Jun. 2022.
[25] A. Kolli, O. Béthoux, A. De Bernardinis, E. Labouré, and G. Coquery, "Space-vector PWM control synthesis for an H-bridge drive in electric vehicles," *IEEE Trans. Veh. Technol.*, vol. 62, no. 6, pp. 2441–2452, Jul. 2013.
[26] P. Sandulescu, F. Meinguet, X. Kestelyn, E. Semail, and A. Bruyère, "Control strategies for open-end winding drives operating in the flux-weakening region," *IEEE Trans. Power Electron.*, vol. 29, no. 9, pp. 4829–4842, Sep. 2014.
[27] H. Zhan, Z. Zhu, and M. Odavic, "Analysis and suppression of zero sequence circulating current in open winding PMSM drives with common DC bus," *IEEE Trans. Ind. Appl.*, vol. 53, no. 4, pp. 3609–3620, Jul./Aug. 2017.
[28] X. Zhang and W. Zhang, "Model predictive full-torque control for the open-winding PMSM system driven by dual inverter with a common DC bus," *IEEE J. Emerg. Sel. Topics Power Electron.*, vol. 9, no. 2, pp. 1541–1554, Apr. 2021.
[29] X. Yuan, S. Zhang, C. Zhang, M. Degano, G. Buticchi, and A. Galassini, "Improved finite-state model predictive current control with zero-sequence current suppression for OEW-SPMSM drives," *IEEE Trans. Power Electron.*, vol. 35, no. 5, pp. 4996–5006, May 2020.
[30] P. Cortes, J. Rodriguez, C. Silva, and A. Flores, "Delay compensation in model predictive current control of a three-phase inverter," *IEEE Trans. Ind. Electron.*, vol. 59, no. 2, pp. 1323–1325, Feb. 2012.
[31] C. K. Lin, J. T. Yu, Y. S. Lai, and H. C. Yu, "Improved model-free predictive current control for synchronous reluctance motor drives," *IEEE Trans. Ind. Electron.*, vol. 63, no. 6, pp. 3942–3953, Jun. 2016.

Xueping Li was born in Shandong, China, in 1994. He received the B.Eng. degree in vehicle engineering from the Chang'an University, Xi'an, China, in 2018. He is currently working toward the Ph.D. degree in mechanical engineering with the National Engineering Laboratory for Electric Vehicles and School of Mechanical Engineering, Beijing Institute of Technology, Beijing, China.

His research interests include predictive control for synchronous motor drives and multiphase motor drives.

Shuo Zhang (Member, IEEE) received the B.Eng. degree in electrical engineering from the North China Institute of Aerospace Engineering, Hebei, China, in 2011, and the Ph.D. degree in vehicle engineering from the Beijing Institute of Technology, Beijing, China, in 2017.

He is currently an Assistant Professor with the National Engineering Laboratory for Electric Vehicles and School of Mechanical Engineering, Beijing Institute of Technology. His research interests include the modeling and control for the permanent magnet synchronous motor, multimotor driving system, and hybrid power system.

Chengning Zhang received the M.E. degree in control theory and control engineering and the Ph.D. degree in vehicle engineering from the Beijing Institute of Technology, Beijing, China, in 1989 and 2001, respectively.

He is currently a Professor and the Vice Director with the National Engineering Laboratory for Electric Vehicles, Beijing Institute of Technology. His research interests include electric vehicles, vehicular electric motor drive systems, battery management systems, and chargers.

Ying Zhou was born in Hebei, China, in 1997. She received the B.Eng. degree in vehicle engineering from the Dalian University of Technology, Dalian, China, in 2018. She is currently working toward the Ph.D. degree in mechanical engineering with the National Engineering Laboratory for Electric Vehicles and School of Mechanical Engineering, Beijing Institute of Technology, Beijing, China.

Her research interests include synchronous motor drives, open winding permanent magnet synchronous motor drives, and parameter identification strategy of motor.

Xin Yuan (Member, IEEE) received the B.S. degree in electrical engineering and automation from Beijing Union University, Beijing, China, in 2013 and M.S. degree in electrical engineering from North China University of Technology, Beijing, China, in 2016, and the Ph.D. degree in electrical engineering from the Beijing Institute of Technology, Beijing, China, in 2020.

He was a Research Associate with the PEMC Group, University of Nottingham, Nottingham, U.K., from 2019 to 2020, before joining the Hong Kong Polytechnic University, Hong Kong. In 2020, he was a Postdoctoral Research Fellow with the School of Electrical and Electronic Engineering, Nanyang Technological University, Singapore. He currently joined the Department of Electrical Engineering, Hong Kong Polytechnic University, as a Research Assistant Professor in June 2022. He has authored/coauthored more than 30 papers and served as a Reviewer for more than 20 international journals. His research interests include ac motor drives in transportation applications, power converters, wireless power transfer, model predictive control, and control theory.

Dr. Yuan was the recipient of many awards, including the best Ph.D. thesis award, outstanding Ph.D. graduate award, first honor academic scholarship, SMC scholarship, national inspirational scholarship, etc.

Yuelin Dong received the B.Eng. degree in vehicle engineering from the Beijing Forestry University, Beijing, China, in 2019. He is currently working toward the Ph.D. degree in mechanical engineering with the Collaborative Innovation Center for Electric Vehicles and School of Mechanical Engineering, Beijing Institute of Technology, Beijing, China.

His research interest includes permanent magnet synchronous motor drive.